



Stress evolution in top coat of thermal barrier coatings by considering strength difference property in tension and compression



C. Lin^{a,b}, Sun Qiang^{b,c}, Chai Yijun^{b,c}, Chen Hualing^{a,b}, Li Yueming^{b,c,*}

^a School of Mechanical Engineering, Xi'an Jiaotong University, Xi'an 710049, China

^b State Key Laboratory for Strength and Vibration of Mechanical Structures, Xi'an Jiaotong University, Xi'an 710049, China

^c School of Aerospace Engineering, Shaanxi Key Laboratory of Environment and Control for Flight Vehicle, Xi'an Jiaotong University, Xi'an 710049, China

ARTICLE INFO

Article history:

Received 12 April 2017

Revised 27 June 2017

Accepted in revised form 20 July 2017

Available online 21 July 2017

Keywords:

Top coat (TC)

Stresses evolution

Strength difference property

ABSTRACT

The experimental research shows that ceramic top coat (TC) exhibits obvious strength difference (SD) in tension and compression, called SD property. This property significantly affect stress evolution, however, there are few attentions to it. In this paper, the stress evolution in TC layer is investigated by considering SD property. To reflect its property, a return mapping algorithm model for unified strength theory (UST), proposed by us, is applied. The results reveal that SD property leads to the movement of maximum tensile stress from interface to the position above it. It suggests that the crack might not be directly initiated at interface but above it, which has been reported in experimental studies too. The results also reveal that the possibility of above-interface cracking could be increased by varying the material properties, such as elevating compressive-tensile strength ratio and reducing yield strength of TC, and by changing the coating geometries, such as thickening thermally grown oxide (TGO) layer and increasing TC interfacial amplitude-wavelength ratio.

© 2017 Elsevier B.V. All rights reserved.

1. Introduction

Ceramic top coat (TC), acting as thermal insulation, is one of the indispensable elements for thermal barrier coatings (TBC). It, typically made of 7 wt% Y₂O₃-stabilized ZrO₂ (YSZ), has one of the lowest thermal conductivities at high temperature for ceramics [1], enabling gas turbine and aero-engine to service at the gas temperature well above super-alloy's melting temperature. Currently, air plasma spray deposition (APS) and electron beam physical vapor deposition (EB-PVD) are the two most important methods for depositing ceramic top coat onto metal substrates. The high-cost EB-PVD TC, in which the grains of ceramic form in a columnar manner perpendicular to TC-bond coat (BC) interface, provides higher strain tolerance in service and is usually reserved for aerospace industry. The low-cost APS TC, having lower strain tolerance but providing higher thermal resistance, is often deposited onto the components of land based gas turbine. EB-PVD and APS top coats exhibit significant difference in mechanical behavior due to the distinct microstructures. In present paper, the study is limited to APS TC.

APS TC is designed not only to have excellent thermal resistance but also to maintain thermal resistance for prolonged service times without failure. Its practical application, however, is seriously restricted by

premature failure. The stress, generated in TC, is considered to be primarily responsible for the premature failure, which induces damage initiation and progression and finally leads to ultimate spallation [2,3]. The accurate prediction of stress in APS TC partly relies on the reasonable characterization of mechanical behaviors.

Different from EB-PVD TC, which has the columnar microstructure, exhibiting significant anisotropic behavior, APS TC has the lamellar microstructure, where pores and cracks randomly distribute. Therefore, for simplicity, APS TC is usually assumed to be isotropic elastic material [4–9]. At elevated temperature, ceramic material exhibits time-dependent inelastic behavior, so creep model rather than elastic model is used to characterize the mechanical behavior of TC in some researches [10–15]. At high temperature, the sintering, resulting from the healing of micro crack and defect, effects the mechanical behavior of APS TC too, which is considered in some researches of stress evolution or cracking behavior by establishing a kind of brick model [16–18], where the sintered APS TC is treated as the anisotropic material. The experimental observation reported by LU et al. [19] confirms that sintering leads to the spheroidization of pore, so that the microstructure is regarded as a homogeneous material with random spherical pores and sintered TC is considered to be isotropic in their researches.

Although several important contributions have been made as mentioned above, a reasonable research still needs to be done for the characterization of mechanical behaviors of TC. For ceramic material, there is an obvious difference between compressive and tensile yield strength. This is called the strength differences property or SD property

* Corresponding author at: State Key Laboratory for Strength and Vibration of Mechanical Structures, Xi'an Jiaotong University, Xi'an 710049, China.

E-mail address: liyueming@xjtu.edu.cn (Y. Li).

[20]. The experimental research [21,22] shows that the compressive strength of ceramic coating is 10 times greater than its tensile strength. The SD property of ceramic coating might significantly affect the stress evolution in TC layer, however, there are few attentions to it. Thus, the purpose of this paper is to develop a numerical approach to investigate the stress evolution in TC layer by considering SD property. In this paper, TC is treated as the elastic perfect plastic material with SD properties, and the creep property and sintering effect are ignored for simplicity. To reflect SD property, a return mapping algorithm model in principal stress space for unified strength theory (UST), proposed by us [23], is used. In addition, the combined creep-plastic constitutive relationship [24] is employed to characterize the material behaviors of thermally grown oxide (TGO) and BC, and the diffusion oxidation reaction scheme [24] is applied to describe TGO growth.

2. Methodology

2.1. Return mapping algorithm model for UST to describe plastic behavior of TC with SD property

In this paper, unified strength theory (UST), proposed by Yu [20], which could comprehensively consider the basic material characteristics, including SD property, hydrostatic-stress effect and intermediate-principal-stress effect, is employed for the description of plastic behavior of TC. The mathematical formulation of UST, in the sextant of principal stress space $\sigma_1 \geq \sigma_2 \geq \sigma_3$, is given as follows,

$$F \equiv \sigma_1 - \frac{\alpha}{1+b} (b\sigma_2 + \sigma_3) = \sigma_t, \quad \text{when } \sigma_2 \leq \frac{\sigma_1 + \alpha\sigma_3}{1+\alpha} \quad (1)$$

$$F' \equiv \frac{1}{1+b} (\sigma_1 + b\sigma_2) - \alpha\sigma_3 = \sigma_t, \quad \text{when } \sigma_2 \geq \frac{\sigma_1 + \alpha\sigma_3}{1+\alpha} \quad (2)$$

where σ_t is tensile yield strength, α is tensile-compressive strength ratio to reflect SD property and b is a parameter that describes the effect of intermediate principal stress on the failure of material.

As shown in Fig. 1, the yield surfaces of UST are piecewise-linear including corners and apex, so that the orthogonal flow rule by Koiter [25] is not appropriate at the corners and apex, which leads to numerical singularity. To eliminate the numerical singularity, Yu [26] introduces an explicit Euler algorithm model, in which the average of piecewise-linear yield function flow vectors is used at the corners. What is lacking is that the updated stress might not satisfy the yield condition strictly and the accuracy of numerical solution is strongly dependent on the iteration step length.

Recently a return mapping algorithm model in principal stress space for UST is proposed by us [23]. In the proposed model, the stress-updates are carried out in principal stress space, so that the plastic flow vectors at the corners and apex can be easily and exactly determined based on Koiter's theory. In addition, the proposed model is a kind of implicit Euler algorithm model, which has the advantages of good calculation accuracy, unconditional stability and quadratic rate of convergence. The details of the derivation of the algorithm model is proposed in Ref. [23], in this paper only the brief processes of stress-update in principal stress space are introduced for simplicity (see Appendix A).

2.2. Combined creep-plastic constitutive relationship for TGO and BC

In this paper, the deformation behaviors of TGO and BC are characterized by the combined creep-plastic constitutive model, introduced by us [24], as follows,

$$\begin{aligned} \boldsymbol{\varepsilon}_{TGO} &= \boldsymbol{\varepsilon}_{TGO}^{th} + \boldsymbol{\varepsilon}_{TGO}^e + \boldsymbol{\varepsilon}_{TGO}^p + \boldsymbol{\varepsilon}_{TGO}^c + \boldsymbol{\varepsilon}_{TGO}^g \\ \boldsymbol{\varepsilon}_{BC} &= \boldsymbol{\varepsilon}_{BC}^{th} + \boldsymbol{\varepsilon}_{BC}^e + \boldsymbol{\varepsilon}_{BC}^p + \boldsymbol{\varepsilon}_{BC}^c \end{aligned} \quad (3)$$

where the subscripts TGO and BC, respectively, represent the TGO and BC materials; $\boldsymbol{\varepsilon}^{th}$ is thermal strain; $\boldsymbol{\varepsilon}^g$ represents permanent volumetric

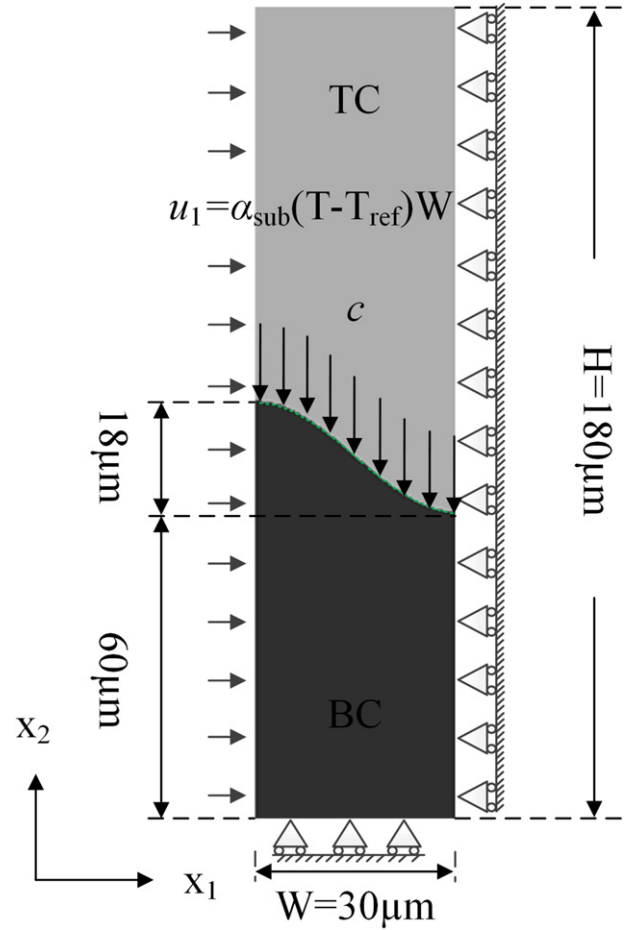


Fig. 1. Boundary condition.

swelling strain; $\boldsymbol{\varepsilon}^p$ is plastic strain, which is derived from the plastic flow rule based on von-Mises yield criterion; $\boldsymbol{\varepsilon}^c$ is creep strain. Norton-type creep strain rate [28] is adopted in the form,

$$\dot{\boldsymbol{\varepsilon}}^c = A[q(\boldsymbol{\sigma})]^\rho \exp\left(\frac{-Q}{R(T+273)}\right) \quad (4)$$

where $\dot{\boldsymbol{\varepsilon}}^c$ is equivalent creep strains rate; $q(\boldsymbol{\sigma})$ is equivalent stress; A, ρ, Q, R, T are, respectively, reference creep strain rate, creep exponent, creep activation energy, ideal gas constant and Celsius temperature.

2.3. Diffusion-oxidation reaction scheme for TGO growth

In this paper, a diffusion-oxidation reaction scheme, proposed by us [24], is adopted to simulate TGO growth. In the diffusion-oxidation reaction scheme, TGO-BC interface is assumed to be a gradually moving oxidation front, in which TGO and BC phases coexist,

$$f_{BC} + f_{TGO} = 1 \quad (5)$$

where f represents dimensionless molar fraction. In the oxidation front, Voigt's homogenization assumption [29] is utilized to characterize the mechanics behavior, as follows,

$$\boldsymbol{\varepsilon} = \boldsymbol{\varepsilon}_{BC} = \boldsymbol{\varepsilon}_{TGO} \quad (6)$$

$$\boldsymbol{\sigma} = (1-\xi)\boldsymbol{\sigma}_{BC} + \xi\boldsymbol{\sigma}_{TGO} \quad (7)$$

where $\xi = f_{TGO}$ is the dimensionless molar fraction of TGO. Substituting the Eq. (3) and the Eq. (6) into the Eq. (7), the constitutive relationship in oxidation front is derived,

$$\sigma = (1-\xi)D_{BC}^e : (\epsilon - \epsilon_{BC}^{th} - \epsilon_{BC}^p - \epsilon_{BC}^c) + \xi D_{TGO}^e : (\epsilon - \epsilon_{TGO}^{th} - \epsilon_{TGO}^p - \epsilon_{TGO}^c - \epsilon_{TGO}^g) \quad (8)$$

In the simulation, ξ varies from 0 to 1 to describe oxidation process. The rate of ξ represents oxidation rate, which is assumed to be controlled by the concentration of mobile oxygen anions c and the available BC material, in the form of $\dot{\xi} = \gamma(1-\xi)c$. γ is a constant which needs to be calibrated from oxidation data.

To determine the distribution of concentration of oxygen anions, a modified Fick's law is introduced in the form,

$$\dot{c} = D \operatorname{div}(\nabla c) + S(c) \quad (9)$$

where div and ∇ are, respectively, the divergence operator and gradient operator; D is oxygen anion diffusion coefficient, in the form of $D = (1-\xi)D_{BC} + \xi D_{TGO}$. The oxygen anion diffusion coefficient is considered to be temperature-dependent,

$$D = D_0 \exp\left(-\frac{Q_d}{R(T+273)}\right) \quad (10)$$

where D_0 and Q_d are, respectively, reference oxygen anion diffusion coefficient and oxygen anion diffusion activation energy.

$S(c)$ represents moles of oxygen anion consumed per unit time and volume during oxidation, expressed as follows,

$$S(c) = -\kappa \dot{\xi} \quad (11)$$

where κ is the moles of oxygen anion consumed to generate unit molar volume TGO.

3. Numerical analysis

Based on the methodology presented in Section 2, a self-development user-defend-element (UEL) subroutine is compiled for the simulation of stress evolution considering SD property. In present simulation, the boundary condition is identical to that in Ref. [24]. For simplicity, only the diagrammatic sketch of boundary condition and geometry of FE mesh is illustrated in Fig. 1.

In Fig. 1, u_1 is to reflect the influence of thermal contraction of substrate; α_{sub} is the thermal expansion coefficient of substrate identical to that in Ref. [24]; $T_{ref} = 1100$ °C. TC is assumed to be elastic perfect plastic material with SD property. The mechanical parameters of TC are listed in Table 1. σ_c , in Table 1, represents the compressive yield strength. BC and TGO are assumed to be the materials which exhibit creep and plastic behaviors. Their mechanical parameters are consistent with those in Ref. [24]. The diffusion and oxidation parameters from [31–32] are listed in Table 2.

Table 1
Mechanical parameters of TC.

T (°C)	TC				
	E (GPa) [30]	ν [30]	α ($10^{-6}/^\circ\text{C}$) [30]	σ_t (GPa) [21]	σ_c (GPa) [21]
20	48	0.1	9.7	0.040	0.172
200	47	0.1	9.8	–	–
400	44	0.1	9.9	–	–
600	40	0.11	9.9	–	–
800	34	0.11	10	–	–
1000	26	0.12	10.1	–	–
1100	22	0.12	10.1	–	–

Table 2
Diffusion and oxidation parameters.

	Parameter	Value
Reference diffusion coefficient of oxygen in BC [31]	$D_{0, BC}$ (m^2/s)	7.5×10^{-9}
Reference diffusion coefficient of oxygen in TGO [31]	$D_{0, TGO}$ (m^2/s)	7.5×10^{-9}
Oxygen anion diffusion activation energy of BC [31]	$Q_{d, TGO}$ (kJ/mol)	100
Oxygen anion diffusion activation energy of TGO [31]	$Q_{d, TGO}$ (kJ/mol)	100
Ideal gas constant	R (kJ/(mol \times K))	8.13×10^{-3}
Moles of oxygen anion consumed to generate unit volume TGO [32]	κ (mol/ m^3)	0.24×10^6

The parameter γ , appearing in the Eq. (11), is chosen to be $1.25 \times 10^{-4} \text{ m}^3 / (\text{mol} \times \text{s})$ [24].

TBC is assumed to be exposed at 1100 °C for 300 h, and then cooled down to 20 °C within 120 s. At elevate temperature, the sizable creep deformations of TGO and BC effectively relax stress and lead to an approximate zero-stress state in TBC throughout this stage [10,24]. Since the zero-stress state could not induce plastic deformation and not affected by SD property, the stress evolution, at cooling stage rather than high temperature stage, is investigated in present paper.

At cooling, stress evolution in TC is mainly affected by thermal expansion mismatch among TC, TGO, BC layers. TGO has the smallest thermal expansion coefficient (see Tables 1 and 2), therefore the thermal expansion mismatch among the three layers could induce compressive stress in TGO layer. The compressive stress, in TGO layer, motives itself out-of-plane deformation, which leads to the accumulation of tensile stress at valley region and compressive stress at peak region of TC. The thermal expansion mismatch between substrate and TBC, inducing a contraction of TBC in x_1 direction, also enhances the out-of-plane deformation of TGO and elevates the stress-level in TC layer. In addition, the Young's modulus increasing, at cooling stage, leads to a further increase of stress-level in TC layer.

The contour plots of stress σ_{22} , at 20 °C, are illustrated in Fig. 2. Here, TC is assumed to be elastic, elastic perfect plastic without SD property ($\sigma_t = \sigma_c = 0.172$ GPa) and elastic perfect plastic with SD property ($\sigma_t = 0.04$ GPa, $\sigma_c = 0.172$ GPa), respectively. The significant difference is found in the stress magnitude between the simulation results considering SD property and not. Taking SD property into account, the considerable plastic deformation occurs in TC layer, which effectively reduces the stress-level. Another deference should be noted that the maximum tensile stress is above interface rather than at interface when SD property is considered. In general, the location of maximum tensile stress is consistent with the location of crack initiation. It means that the crack initiation might be not at interface but above it. Although it is not reported in current numerical studies, the experimental research [33,34] shows that the crack indeed not initiate directly at the interface but above it.

The evolution of stress σ_{22} , in TC layer at cooling stage, is illustrated in Fig. 3. It is observed that at the end of cooling stage the maximum tensile stress moves from the location above interface to the location at interface when SD property is ignored (as shown in Fig. 3(d) and (e)), while the maximum tensile stress is above interface and its location remains unchanged when SD property considered (as shown in Fig. 3(i) and (j)).

SD property leads to the result that plastic yielding occurs more easily in tension than in compression. It is observed that the relative low tensile stress state induces plastic deformation by considering SD property (as shown in Fig. 4(a) and (b)), while TC layer is mainly in elastic state when SD property is ignored (as shown in Fig. 4(c) and (d)). The plastic deformation, induced by tensile stress, is at the location above interface (as shown in Fig. 4(a) (b)), which is consistent with the location of maximum tensile stress (as shown in Fig. 3(j)). With the stress evolution, the plastic zone extends in the negative x_1 direction as shown

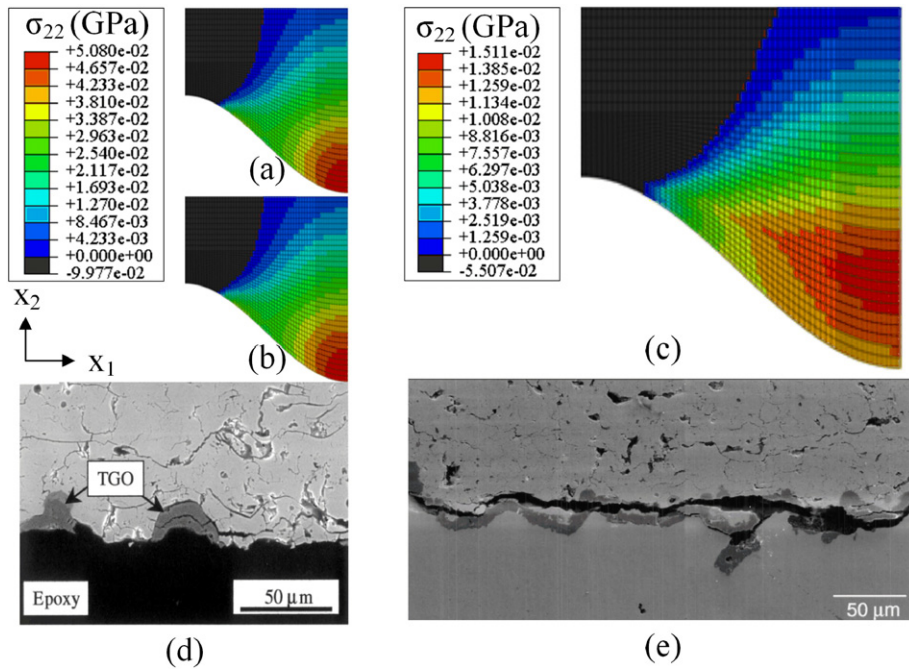


Fig. 2. Contour plots of stress σ_{22} , after 300 hour oxidation at 20 °C, under the (a) elastic, (b) elastic perfect plastic without SD property ($\sigma_t = \sigma_c = 0.172\text{GPa}$) and (c) elastic perfect plastic with SD property ($\sigma_t = 0.04\text{GPa}$, $\sigma_c = 0.172\text{GPa}$) assumptions of TC; failure mode in APS TC reported in (d) [34] and (e) [33].

in Fig. 4(b), which is consistent with the experimentally observed crack propagation path [33,34] (as shown in Fig. 2(d) and (e)). Since the extension of plastic zone weakens the local deformation resistance and leads to stress redistribution, a stress concentration similar to that around defect or crack occurs at the location above interface, as shown in Fig. 3(i) and (j), which leads to the result that maximum tensile stress is not at interface but above it.

In addition, it is noticed that a large plastic deformation is also observed near the peak region of interface, as shown in Fig. 4(a) and (b). The plastic deformation near the peak region, however, is not mainly induced by tensile but compressive stress. Although materials can fail in compression, tensile loading is perhaps more critical, therefore the

plastic deformation, induced by compressive stress, is not considered here.

3.1. Influence of material properties on stress

In general, there exist significant differences in SD properties of ceramic material due to the variation in porosity, particle size, material component or temperature. The experimental result shows that the tensile-compressive strength ratio α is 0.232 at 20 °C and 0.270 at 1100 °C. Ref. [21,22] report that the tensile-compressive strength ratio α of ceramic materials is about 0.1. To reflect the difference in SD property, a simulation, in which the tensile strength σ_t is kept constant and

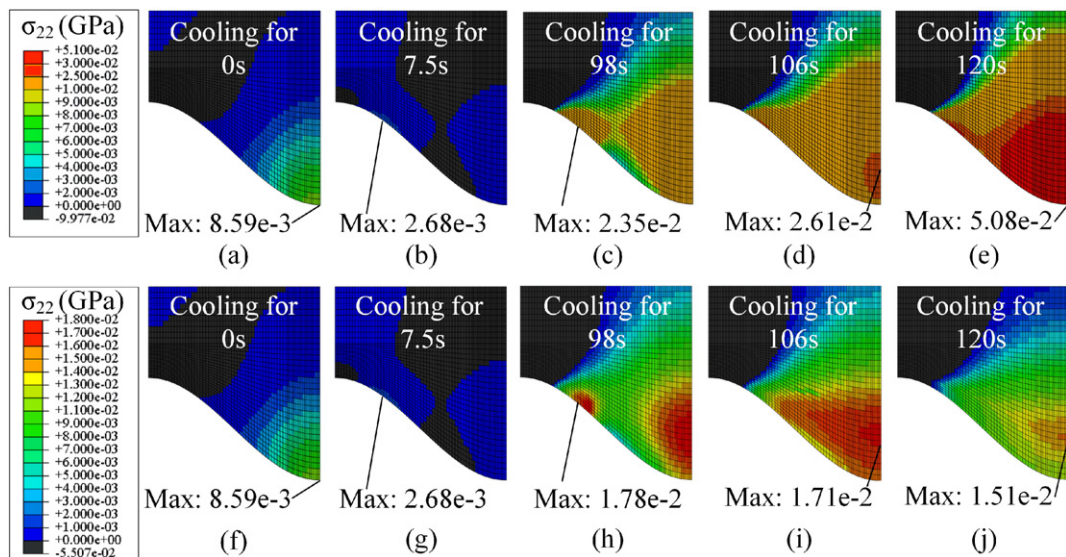


Fig. 3. Evolution of stress σ_{22} with cooling under the (a)–(e) elastic perfect plastic without SD property ($\sigma_t = \sigma_c = 0.172\text{GPa}$) and (f)–(j) elastic perfect plastic with SD property ($\sigma_t = 0.04\text{GPa}$, $\sigma_c = 0.172\text{GPa}$) assumptions of TC.

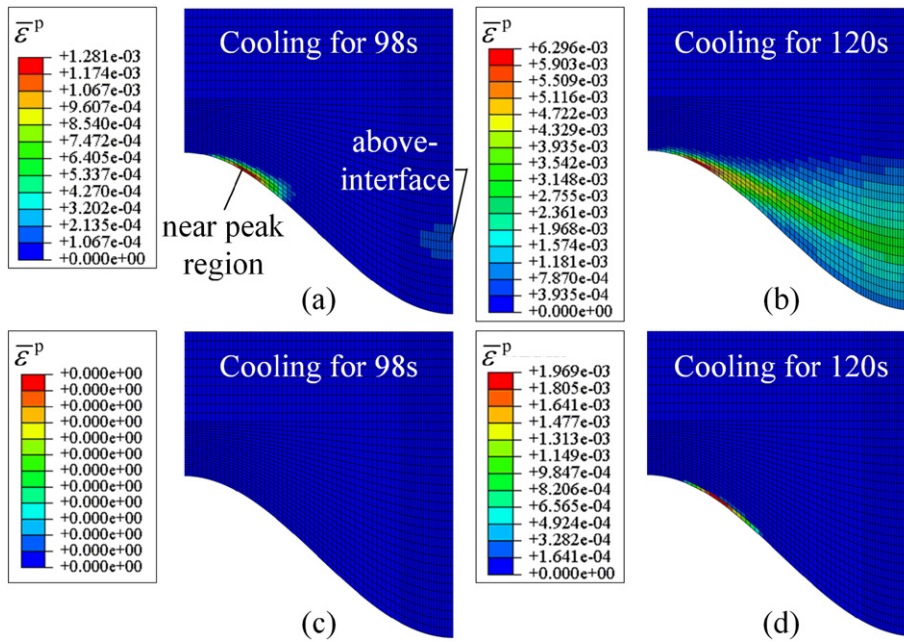


Fig. 4. Evolution of equivalent plastic strain with cooling under the condition that (a) and (b) SD property is considered, (c) and (d) ignored.

the tensile-compressive strength ratio α varies from 0.1 to 1, is carried out.

The contour plots of stress σ_{22} with tensile-compressive strength ratio α are illustrated in Fig. 5. With α decreasing, maximum tensile stress moves from interface to the location above it, which once again suggests that SD property of TC leads to the movement of maximum tensile stress.

The tensile stress versus $1/\alpha$ relation curves are plotted in Fig. 6(a). When $1/\alpha$ is smaller than 2.5, the tensile stress above interface is lower than that at interface. It suggests that the maximum tensile stress is at interface and the crack tends to initiate at interface. When the $1/\alpha$ is larger than 2.5, an opposite result is observed that the stress above interface is higher than that at interface. It means that the crack, induced by tensile stress, might not initiate at interface but above it. Since the

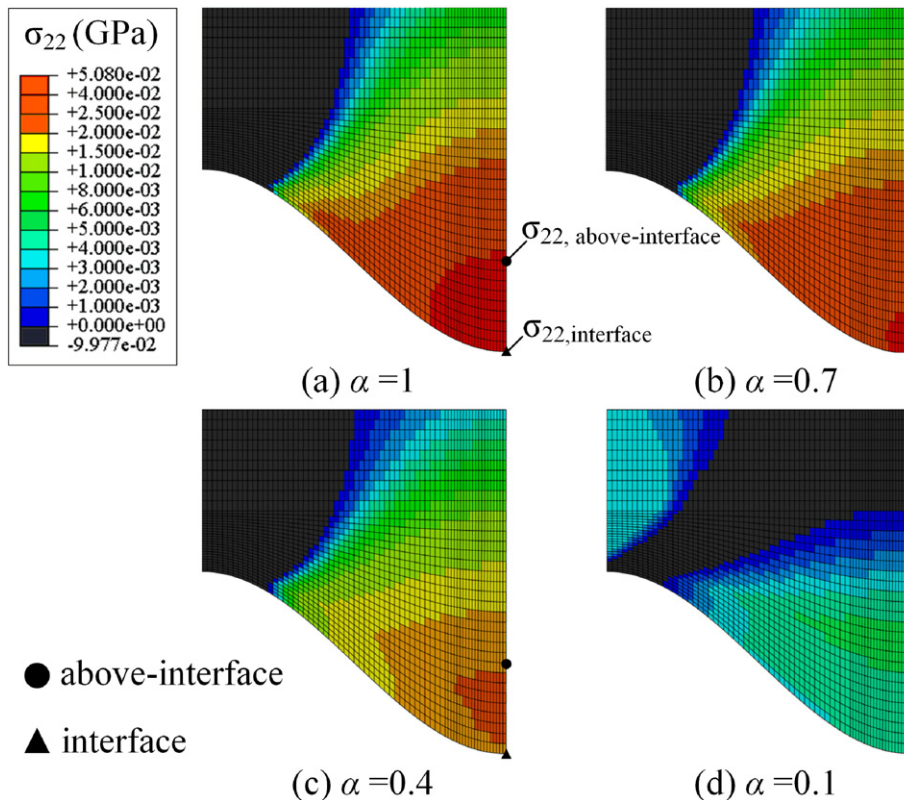


Fig. 5. Contour plots of stress σ_{22} with tensile-compressive strength ratio α .

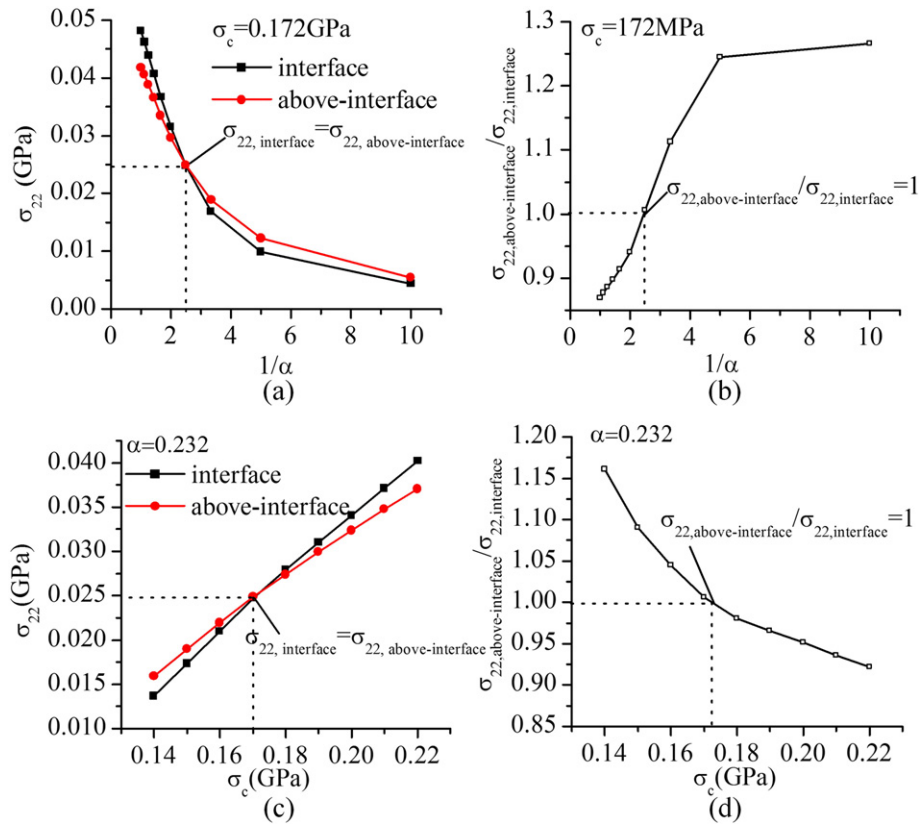


Fig. 6. Evolution of (a) stress σ_{22} and (b) stress-ratio $\sigma_{\text{above-interface}}/\sigma_{\text{interface}}$ under the condition that $\sigma_c = 0.172$ GPa, and Evolution of (c) stress σ_{22} and (d) stress-ratio $\sigma_{\text{above-interface}}/\sigma_{\text{interface}}$ under the condition that $\alpha = 0.232$.

fracture toughness of interface is usually lower than that of TC itself, the position displacement of maximum tensile does not necessarily lead to the cracking above interface.

The evolution of the ratio between stresses above interface and at interface is illustrated in Fig. 6(b), which shows an increasing tendency of stress ratio with the increase of $1/\alpha$. It suggests that increase of $1/\alpha$ enhances the stress concentration at the location above interface, which elevates the possibility of above-interface cracking.

With the variation in porosity, particle size, material component or temperature, the yield strength also varies. To investigate yield strength influence on stress evolution, a simulation, in which the

tensile-compressive strength ratio $\alpha = 0.232$ is kept constant and compressive strength σ_c varies from 0.140 to 0.220 GPa, is implemented. The stress evolution, shown in Fig. 6(c) and (d), exhibits a similar pattern to that in Fig. 6(a) and (b), which suggests that the decrease of yield strength elevates possibility of above-interface cracking.

Since the stress evolution is affected by not only SD property but yield strength, the combined influence of SD property and yield strength is investigated. The relation curves between stress-ratio and $1/\alpha$ under different compressive strength σ_c are plotted in Fig. 7(a).

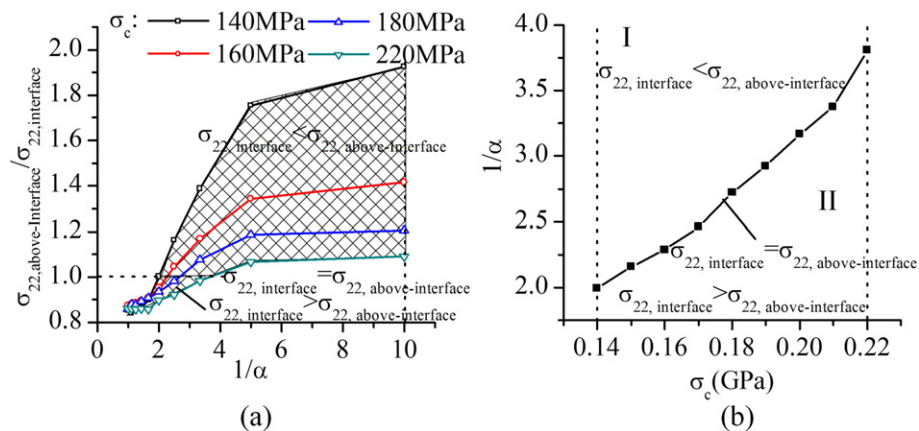


Fig. 7. (a) Relation curves between stress-ratio and $1/\alpha$ under different compressive strength σ_c , and (b) curve relation between $1/\alpha$ and compressive strength σ_c under the condition that stress-ratio $\sigma_{\text{above-interface}}/\sigma_{\text{interface}} = 1$.

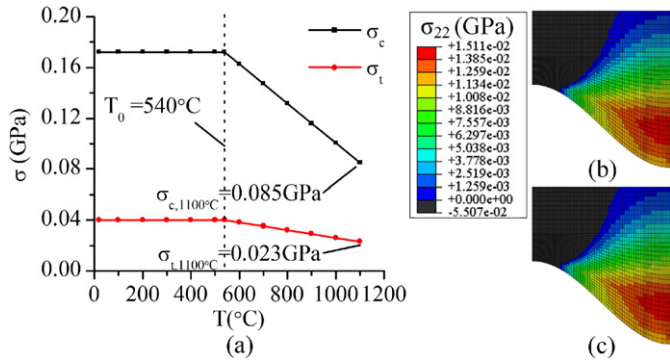


Fig. 8. (a) Evolution of tensile and compressive strength with temperature, and contour plots of stress σ_{22} under perfect elasto-plastic with SD property assumptions of TC by (b) considering temperature dependence and (c) not.

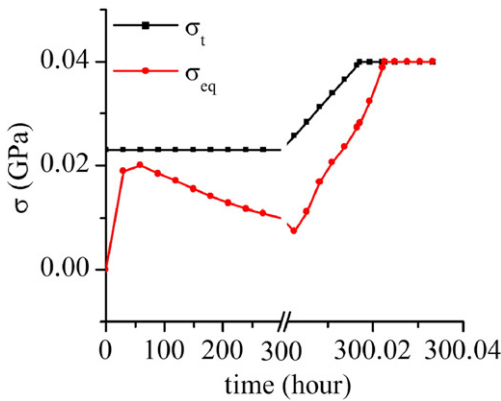


Fig. 9. Evolution of maximum equivalent stress.

Under the condition that stress-ratio $\sigma_{\text{above-interface}}/\sigma_{\text{interface}} = 1$, the curve relation between $1/\alpha$ and compressive strength σ_c is plotted in Fig. 7(b). This curve divides the region, spanning from $\sigma_c = 0.140$ GPa to $\sigma_c = 0.220$ GPa, into two parts. It is observed that the stress $\sigma_{\text{above-interface}}$ is larger than $\sigma_{\text{interface}}$ in part I. It suggests that maximum tensile stress is above interface when the combination of $1/\alpha$ and σ_c is within part I. In this condition, the crack might not directly initiate at interface but above it. Conversely, the stress $\sigma_{\text{above-interface}}$ is small than $\sigma_{\text{interface}}$ in part II. It indicates that maximum tensile stress and the crack initiation are at interface when the combination of $1/\alpha$ and σ_c lies in part II. It is noted that under different compressive strength σ_c , the $1/\alpha$ is always

larger than 1 when the maximum tensile stress is at the location above interface. It suggests that SD property rather yield strength mainly leads to the location movement of maximum tensile.

In a more realistic case, the temperature dependent tensile and compressive strength are considered in the simulation. The evolution of tensile and compressive yield strength with temperature is illustrated in Fig. 8(a), which is from the experimental measured [21]. The result, considering temperature dependence, however, is almost identical to that ignoring it, as shown in Fig. 8(b) and (c).

The evolution of maximum equivalent stress σ_{eq} in TC is illustrated in Fig. 9. It is observed that the maximum equivalent stress is always beneath the yield strength σ_t when the yield strength varies with temperature. Since the temperature dependence of yield strength does not affect the stress evolution, it is ignored in the following simulation.

3.2. Influence of geometrical features on stress

Not only the material properties but also the geometrical features, such as TGO thickness and interface roughness, affect the stress in TC layer.

Since TGO thickness is usually not more than 10 μm , a simulation, where TGO thickness varies from 1 to 9 μm and the interfacial amplitude-wavelength ratio remains unchanged, is carried out to investigate the influence of TGO thickness on stress. As shown in Fig. 1, the interface morphology is idealized as the sinusoidal shape with the amplitude of 18 μm and half-wavelength of 30 μm . Therefore the interfacial amplitude-wavelength ratio is equal to 0.15. SD property is considered and the material parameters of TC are chosen from Table 1. It is observed in Fig. 10 that the stress-level rises and the maximum tensile stress moves from TC peak to valley region with TGO thickening, which is consistent to that reported in Ref. [35]. The difference is that the location of maximum tensile stress is not at interface but above it when the maximum tensile stress is in valley region.

When TGO thickness is more than 3 μm , the evolutions of stress and stress-ratio are, respectively, plotted in Fig. 11(a) and (b). It is obvious that the stress curve $\sigma_{\text{interface}}$ is always beneath the stress curve $\sigma_{\text{above-interface}}$. It suggests that SD property rather than TGO thickening is the primary factor leading to the movement of maximum tensile from interface to above it. The increase of stress and stress-ratio with TGO thickening are observed, which indicates that TGO thickening enhances stress concentration at the location above interface and elevates the possibility of above-interface cracking. The evolution of $\sigma_{\text{interface}}$ exhibits a trend of rise first, and then fall, as shown in Fig. 11(a). It is because that the TGO thickening on one hand elevates stress-level which lead to the increasing of $\sigma_{\text{interface}}$, on the other hand enhances stress concentration above interface which leads to the decreasing of $\sigma_{\text{interface}}$.

To investigate the interface toughness influence, a simulation is carried out, where the interfacial amplitude-wavelength ratio varies from 0.1 to 0.25. TGO thickness is chosen to be 4 μm which is identical to the thickness after 300 hour oxidation [24]. SD property is also

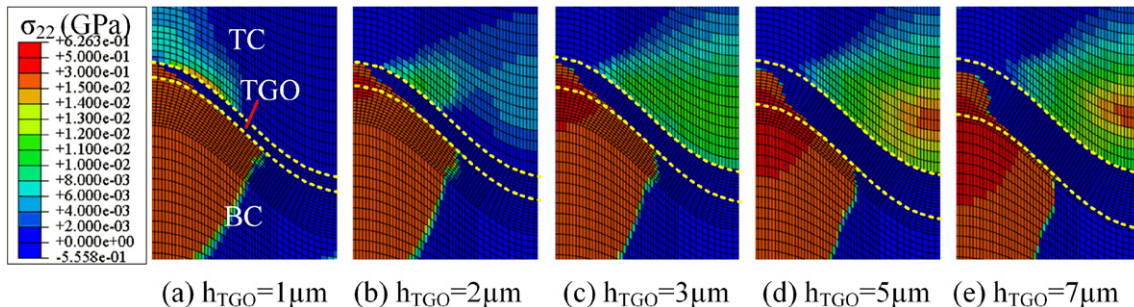


Fig. 10. Contour plots of stress σ_{22} considering different TGO thicknesses.

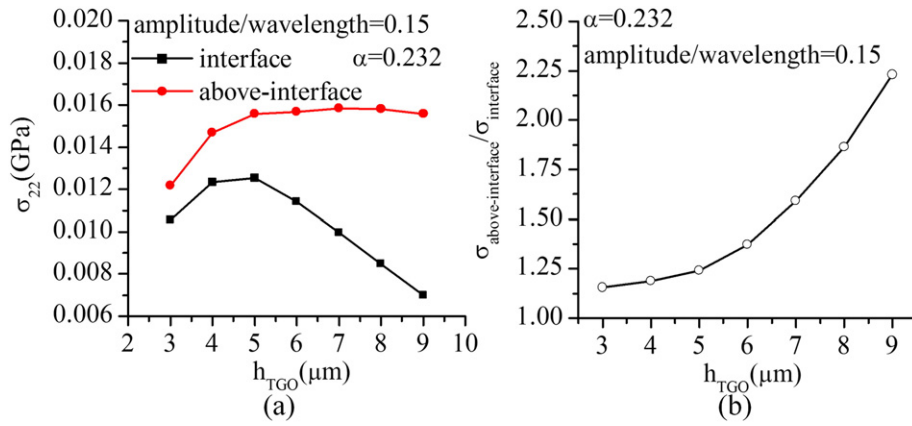


Fig. 11. Evolutions of (a) stress and (b) stress-ratio with TGO thickening.

considered and the material parameters are from Table 1. Under the elastic assumption of TC, the maximum tensile stress, observed in Fig. 12(a), moves from the valley of interface to the peak of interface, which is consistent with that reported in Ref. [36–38].

The difference is that the maximum tensile stress is not at interface but above it by considering SD property, as shown in Fig. 12(b). The evolution of stress σ_{22} and stress-ratio $\sigma_{\text{above-interface}}/\sigma_{\text{interface}}$ with amplitude-wavelength ratio are illustrated in Fig. 13(a) and (b), respectively. With amplitude-wavelength ratio increasing, the more obvious stress concentration at the location above interface is also observed, which elevates the possibility of above-interface cracking.

4. Conclusion

In this paper, the stress evolution in TC layer of TBC is studied by considering SD property. A return mapping algorithm model for UST to describe plastic behavior of TC with SD property, and then a self-

development UEL subroutine is compiled. The numerical results reveal that:

The maximum tensile stress, in TC layer, is at the location above interface when SD property is considered. It indicates that the crack initiation might be not at interface but above it, which is also observed in experimental research [33]. The increase of compressive-tensile strength ratio $1/\alpha$ leads to a more significant stress concentration at the location above interface, which elevates the possibility that crack not directly initiates at interface but above it.

Under the condition that SD property is considered, the decrease of yield strength as well as the increase of TGO thickness and interfacial amplitude-wavelength ratio also elevate the above-interface cracking possibility.

Acknowledgements

This work was supported by the National Basic Research Program of China (No. 2013CB035704) and the National Nature Science Foundation of China (No. 11472206). We are grateful for the support.

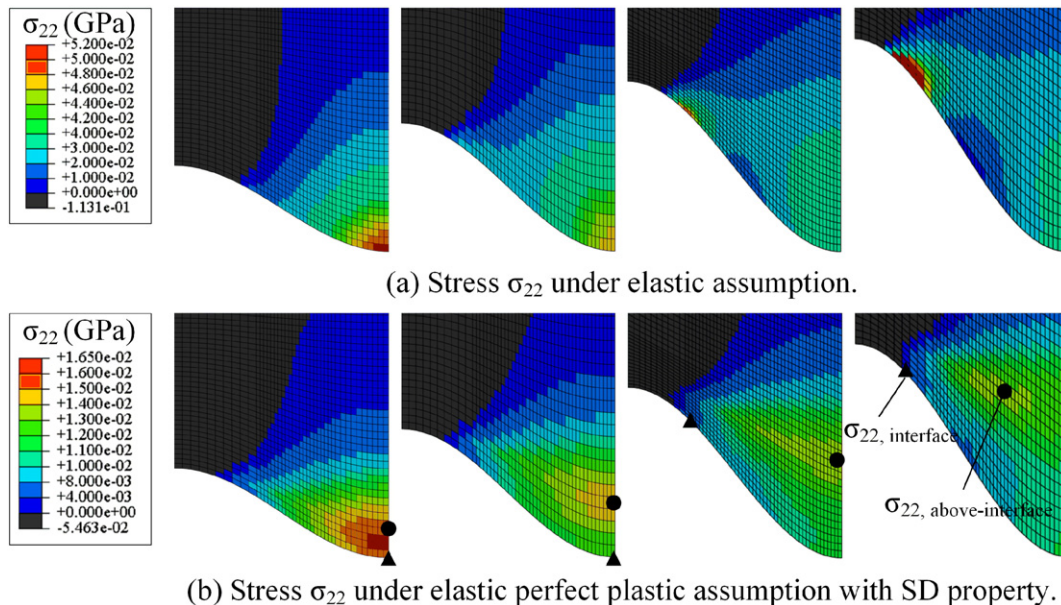


Fig. 12. Contour plots of stress σ_{22} considering different amplitude-wavelength ratios.

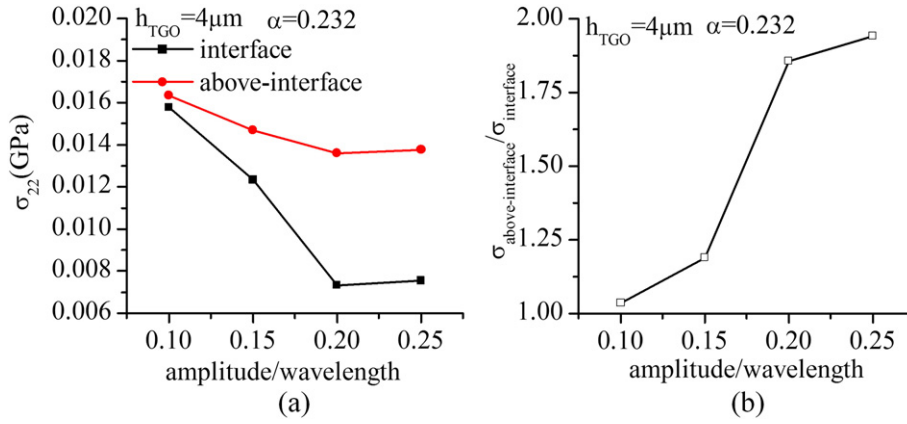


Fig. 13. Evolutions of (a) stress and (b) stress-ratio with amplitude-wavelength ratio.

Appendix A

As illustrated in Fig. A.1(a), there are six different stress-update possibilities in the sextant of principal stress space $\sigma_1 \geq \sigma_2 \geq \sigma_3$ for UST model: stress-updates at the main plane 1, main plane 2, left corner, middle corner and apex. In this paper only the processes of stress-update at main plain 1, middle corner and apex are introduced for simplicity. The associated plastic flow rule, the linear isotropic hardening and the isotropic elasticity are considered.

Stress-update at main plain 1

As shown in Fig. A.1(b), the constitutive relation can be written as follows,

$$\sigma_j = \sigma_j^{\text{tr}} - \Delta\lambda \mathbf{D}_{3 \times 3}^e : \mathbf{N} \tag{A.1}$$

where σ_j^{tr} and σ_j are, respectively, the elastic trial principal stress vector and the updated principal stress vector, $\Delta\lambda$ is the plastic flow parameter, $\mathbf{D}_{3 \times 3}^e$ is the reduced elastic isotropic constitutive matrix, and \mathbf{N} is the reduced plastic flow vector normal to the main plane 1, expressed as,

$$\mathbf{N} = \begin{Bmatrix} 1 \\ -ab/(1+b) \\ -a/(1+b) \end{Bmatrix} \tag{A.2}$$

The updated stresses should lie on the yield surfaces. Substituting the constitutive function Eq. (A.1) into yield function Eq. (1), one obtains,

$$F : \mathbf{N}^T : (\sigma_j^{\text{tr}} - \Delta\lambda \mathbf{D}_{3 \times 3}^e : \mathbf{N}) - (\sigma_t^0 + H\Delta\lambda) = 0 \tag{A.3}$$

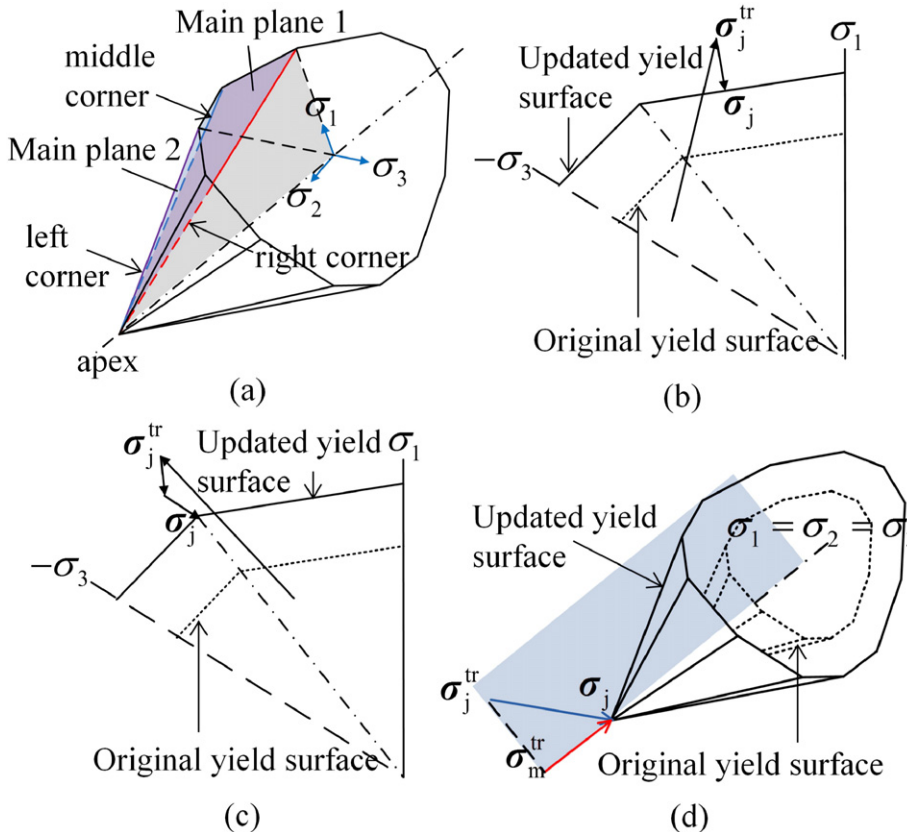


Fig. A.1. (a) UST yield surface in principal stress space and stress-update at (b) main plane 1, (c) middle corner and (d) apex.

where σ_t^0 and H are, respectively, the initial tensile strength and the linear isotropic hardening modulus. From Eq. (A.3), the plastic flow parameter can be derived to be,

$$\Delta\lambda = \frac{\mathbf{N}^T : \boldsymbol{\sigma}_j^{\text{tr}} - \sigma_t^0}{\mathbf{N}^T : \mathbf{D}_{3 \times 3}^e : \mathbf{N} + H} \quad (\text{A.4})$$

Substituting Eq. (A.4) into Eq. (A.1), the updated stresses can be easily obtained.

Stress-update at the middle corner

As shown in Fig. A.1(c), the updated stresses lie on the middle corner. Based on Koiter's theory [25], the constitutive equation can be written as follow,

$$\boldsymbol{\sigma}_j = \boldsymbol{\sigma}_j^{\text{tr}} - \Delta\lambda_1 \mathbf{D}_{3 \times 3}^e : \mathbf{N} - \Delta\lambda_2 \mathbf{D}_{3 \times 3}^e : \mathbf{N}' \quad (\text{A.5})$$

where \mathbf{N}' is the plastic flow vector perpendicular to the main plane 2, expressed as,

$$\mathbf{N}' = \begin{Bmatrix} 1/(1+b) \\ b/(1+b) \\ -a \end{Bmatrix} \quad (\text{A.6})$$

If the updated stresses lie on the middle corner, the consistency condition should be satisfied as follows,

$$\begin{aligned} F : \mathbf{N}^T : \left(\boldsymbol{\sigma}_j^{\text{tr}} - \Delta\lambda_1 \mathbf{D}_{3 \times 3}^e : \mathbf{N} - \Delta\lambda_2 \mathbf{D}_{3 \times 3}^e : \mathbf{N}' \right) - \left[\sigma_t^0 + H(\Delta\lambda^1 + \Delta\lambda^2) \right] &= 0 \\ F' : \mathbf{N}'^T : \left(\boldsymbol{\sigma}_j^{\text{tr}} - \Delta\lambda_1 \mathbf{D}_{3 \times 3}^e : \mathbf{N} - \Delta\lambda_2 \mathbf{D}_{3 \times 3}^e : \mathbf{N}' \right) - \left[\sigma_t^0 + H(\Delta\lambda^1 + \Delta\lambda^2) \right] &= 0 \end{aligned} \quad (\text{A.7})$$

By solving the Eq. (A.7), the plastic flow parameters $\Delta\lambda$ and $\Delta\lambda'$ can be obtained,

$$\begin{Bmatrix} \Delta\lambda_2 \\ \Delta\lambda_2' \end{Bmatrix} = \begin{bmatrix} \mathbf{N}^T : \mathbf{D}_{3 \times 3}^e : \mathbf{N} + H & \mathbf{N}^T : \mathbf{D}_{3 \times 3}^e : \mathbf{N}' + H \\ \mathbf{N}'^T : \mathbf{D}_{3 \times 3}^e : \mathbf{N} + H & \mathbf{N}'^T : \mathbf{D}_{3 \times 3}^e : \mathbf{N}' + H \end{bmatrix}^{-1} \begin{Bmatrix} \mathbf{N}^T : \boldsymbol{\sigma}_j^{\text{tr}} \\ \mathbf{N}'^T : \boldsymbol{\sigma}_j^{\text{tr}} \end{Bmatrix} \quad (\text{A.8})$$

Substituting $\Delta\lambda$ and $\Delta\lambda'$ into Eq. (A.8), the explicit expression of updated stresses can be derived easily.

Stress-update at the apex

As shown in Fig. A.1(d), the apex of UST model is along the hydrostatic axis ($\sigma_1 = \sigma_2 = \sigma_3$), substituting $\sigma_1 = \sigma_2 = \sigma_3$ into Eqs. (1) or (2), the yield function can be rewritten as,

$$(1-\alpha)\sigma_m = \sigma_t, \quad \text{when } \sigma_1 = \sigma_2 = \sigma_3 \quad (\text{A.9})$$

where $\sigma_m = (\sigma_1 + \sigma_2 + \sigma_3)/3$. At the apex, the general constitutive equation for return mapping is given by Perić and Neto [27] as follows,

$$\sigma_m = \sigma_m^{\text{tr}} - K\Delta\varepsilon_V^p \quad (\text{A.10})$$

where $\Delta\varepsilon_V^p$ is the volumetric plastic strain increment. For UST model, $\Delta\varepsilon_V^p$ is written as,

$$\Delta\varepsilon_V^p = (1-a)\Delta\bar{\varepsilon}^p \quad (\text{A.11})$$

where $\Delta\bar{\varepsilon}^p$ is the equivalent plastic strain increment. Substituting Eqs. (A.10) and (A.11) into Eq. (A.9), one obtains,

$$(1-\alpha)\sigma_m^{\text{tr}} - \sigma_t^0 - \left[K(1-a)^2 + H \right] \Delta\bar{\varepsilon}^p = 0 \quad (\text{A.12})$$

Integrating the Eqs. (A.10), (A.11) and (A.12), the explicit formulation of updated stresses are derived as follows,

$$\sigma_1 = \sigma_2 = \sigma_3 = \frac{H}{K(1-a)^2 + H} \sigma_m^{\text{tr}} + \frac{K(1-a)\sigma_t^0}{K(1-a)^2 + H} \quad (\text{A.13})$$

References

- [1] D.R. Clarke, M. Oechsner, N.P. Padture, Thermal-barrier coatings for more efficient gas-turbine engines, *MRS Bull.* 37 (2012) 891–898.
- [2] S. Ahmadian, E.H. Jordan, Explanation of the effect of rapid cycling on oxidation, rumpling, microcracking and lifetime of air plasma sprayed thermal barrier coatings, *Surf. Coat. Technol.* 244 (2014) 109–116.
- [3] V. Kumar, K. Balasubramanian, Progress update on failure mechanisms of advanced thermal barrier coatings: a review, *Prog. Org. Coat.* 90 (2016) 54–82.
- [4] N.A. Fleck, A.C.F. Cocks, S. Lampenscherf, Thermal shock resistance of air plasma sprayed thermal barrier coatings, *J. Eur. Ceram. Soc.* 34 (2014) 2687–2694.
- [5] L. Yang, F. Yang, Y. Long, Y. Zhao, X. Xiong, X. Zhao, P. Xiao, Evolution of residual stress in air plasma sprayed yttria stabilised zirconia thermal barrier coatings after isothermal treatment, *Surf. Coat. Technol.* 51 (2014) 98–105.
- [6] L. Su, W. Zhang, Y. Sun, T.J. Wang, Effect of TGO creep on top-coat cracking induced by cyclic displacement instability in a thermal barrier coating system, *Surf. Coat. Technol.* 254 (2014) 410–417.
- [7] W. Zhu, L. Yang, J.W. Guo, Y.C. Zhou, C. Lu, Determination of interfacial adhesion energies of thermal barrier coatings by compression test combined with a cohesive zone finite element model, *Int. J. Plast.* 64 (2015) 76–87.
- [8] P. Skalka, K. Slámečka, J. Pokluda, L. Čelko, Stability of plasma-sprayed thermal barrier coatings: the role of the waviness of the bond coat and the thickness of the thermally grown oxide layer, *Surf. Coat. Technol.* 274 (2015) 26–36.
- [9] Q.M. Yu, H.L. Zhou, L.B. Wang, Influences of interface morphology and thermally grown oxide thickness on residual stress distribution in thermal barrier coating system, *Ceram. Int.* 42 (2016) 8338–8350.
- [10] J. Rösler, M. Bäker, K. Aufzug, A parametric study of the stress state of thermal barrier coatings: part I: creep relaxation, *Acta Mater.* 52 (2004) 4809–4817.
- [11] M. Bäker, J. Rösler, G. Heinze, A parametric study of the stress state of thermal barrier coatings part II: cooling stresses, *Acta Mater.* 53 (2005) 469–476.
- [12] P. Seiler, M. Bäker, J. Rösler, Multi-scale failure mechanisms of thermal barrier coating systems, *Comput. Mater. Sci.* 80 (2013) 27–34.
- [13] K. Al-Athel, K. Loeffel, H. Liu, L. Anand, Modeling decohesion of a top-coat from a thermally-growing oxide in a thermal barrier coating, *Surf. Coat. Technol.* 222 (2013) 68–78.
- [14] L. Wang, J.S. Yang, J.X. Ni, C.G. Liu, X.H. Zhong, F. Shao, H.Y. Zhao, S.Y. Tao, Y. Wang, Influence of cracks in APS-TBCs on stress around TGO during thermal cycling: a numerical simulation study, *Surf. Coat. Technol.* 285 (2016) 98–112.
- [15] N. Nayebehshae, S.H. Seyedein, M.R. Aboutalebi, H. Sarpooolaky, S.M.M. Hadavi, Finite element simulation of residual stress and failure mechanism in plasma sprayed thermal barrier coatings using actual microstructure as the representative volume, *Surf. Coat. Technol.* 291 (2016) 103–114.
- [16] A. Cipitria, I.O. Golosnoy, T.W. Clyne, A sintering model for plasma-sprayed zirconia TBCs. Part I: free-standing coatings, *Acta Mater.* 57 (2009) 980–992.
- [17] A. Cipitria, I.O. Golosnoy, T.W. Clyne, A sintering model for plasma-sprayed zirconia thermal barrier coatings. Part II: coatings bonded to a rigid substrate, *Acta Mater.* 57 (2009) 993–1003.
- [18] A.C.F. Cocks, N.A. Fleck, S. Lampenscherf, A brick model for asperity sintering and creep of APS TBCs, *J. Mech. Phys. Solids* 63 (2014) 412–431.
- [19] B. Lv, H. Xie, R. Xu, X. Fan, W. Zhang, T.J. Wang, Effects of sintering and mixed oxide growth on the interface cracking of air-plasma-sprayed thermal barrier coating system at high temperature, *Appl. Surf. Sci.* 360 (2016) 461–469.
- [20] M.H. Yu, *Unified Strength Theory and Its Applications*, Springer Science & Business Media 2011.
- [21] J.T. Demasi-Marcin, K.D. Sheffler, S. Bose, Mechanisms of degradation and failure in a plasma-deposited thermal barrier coating, *J. Eng. Gas Turbines Power* 112 (1990) 521–526.
- [22] E.F. Rejda, D.F. Socie, T. Itoh, Deformation behavior of plasma-sprayed thick thermal barrier coatings, *Surf. Coat. Technol.* 113 (1999) 218–226.
- [23] C. Lin, Y.M. Li, A return mapping algorithm for unified strength theory model, *Int. J. Numer. Methods Eng.* 104 (2015) 749–766.
- [24] C. Lin, Y.M. Li, Interface stress evolution considering the combined creep-plastic behavior in thermal barrier coatings, *Mater. Des.* 89 (2016) 245–254.
- [25] W.T. Koiter, Stress-strain relations, uniqueness and variational theorems for elastic-plastic materials with a singular yield surface, *Q. Appl. Math.* 11 (1953) 350–354.
- [26] M.H. Yu, *Generalized Plasticity*, Springer Science & Business Media 2006.
- [27] E.A. de Souza Neto, D. Peric, D.R.J. Owen, *Computational Methods for Plasticity: Theory and Applications*, John Wiley & Sons, 2011.
- [28] J.J. Skrzypek, *Plasticity and Creep. Theory, Examples and Problems*, CRC, London, 1993.
- [29] L. Dormieux, D. Kondo, F.J. Ulm, *Microporo Mechanics*, John Wiley & Sons, Chichester, 2006.
- [30] J. Cheng, E.H. Jordan, B. Barber, M. Gell, Thermal/residual stress in an electron beam physical vapor deposited thermal barrier coating system, *Acta Mater.* 46 (1998) 5839–5850.
- [31] K. Loeffel, L. Anand, Z.M. Gasem, On modeling the oxidation of high-temperature alloys, *Acta Mater.* 61 (2013) 399–424.

- [32] P.N. Quedsted, R.F. Brooks, L. Chapman, R. Morrell, Y. Youssef, K.C. Mills, Measurement and estimation of thermophysical properties of nickel based superalloys, *Mater. Sci. Technol.* 25 (2009) 154–162.
- [33] A. Rabiei, A.G. Evans, Failure mechanisms associated with the thermally grown oxide in plasma-sprayed thermal barrier coatings, *Acta Mater.* 48 (2000) 3963–3976.
- [34] K.W. Schlichting, N.P. Padture, E.H. Jordan, M. Gell, Failure modes in plasma-sprayed thermal barrier coatings, *Mater. Sci. Eng. A* 342 (2003) 120–130.
- [35] J. Rösler, M. Bäker, M. Volgmann, Stress state and failure mechanisms of thermal barrier coatings: role of creep in thermally grown oxide, *Acta Mater.* 49 (2001) 3659–3670.
- [36] M. Białas, Finite element analysis of stress distribution in thermal barrier coatings, *Surf. Coat. Technol.* 202 (2008) 6002–6010.
- [37] E.P. Busso, Z.Q. Qian, M.P. Taylor, H.E. Evans, The influence of bondcoat and topcoat mechanical properties on stress development in thermal barrier coating systems, *Acta Mater.* 57 (2009) 2349–2361.
- [38] M. Ranjbar-Far, J. Absi, G. Mariaux, F. Dubois, Simulation of the effect of material properties and interface roughness on the stress distribution in thermal barrier coatings using finite element method, *Mater. Des.* 31 (2010) 772–781.